Influence of soluble surfactants and deformation on the dynamics of centered bubbles in cylindrical microchannels

Omer Atasi, Benoit Haut, Annaig Pedrono, Benoit Scheid, Dominique Legendre

Influence of Soluble Surfactants and Deformation on the Dynamics of Centered Bubbles in Cylindrical Microchannels

O. Atasi,[*,†,‡] B. Haut,[†] A. Pedrono,[‡] B. Scheid,[†] and D. Legendre[*,‡]

[†]Transfers, Interfaces and Processes (TIPs), Université libre de Bruxelles, 50 Avenue Franklin Roosevelt, 1050 Brussels, Belgium
[‡]Interface, Institut de Mécanique des Fluides de Toulouse (IMFT), Université de Toulouse, CNRS, 31400 Toulouse, France

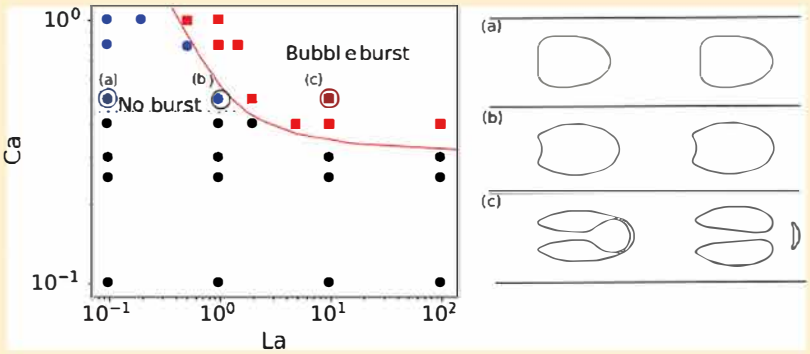

ABSTRACT: In this study, we investigate, using direct numerical simulation, the motion of a small bubble in a horizontal microchannel filled with a liquid containing surfactants. In particular, we study the combined effect of surfactants and bubble deformability on the bubble shape, bubble–liquid relative velocity, velocity field in the liquid, liquid velocity on the gas–liquid interface, and surfactant distribution on the interface. The level set method is used to capture the gas–liquid interface. The surfactant transport equation on the gas–liquid interface is solved in an Eulerian framework and is coupled to an equation describing the transport of surfactants inside the liquid phase. The Marangoni stress, induced by surfactant concentration gradients, is computed using the continuum surface force model. The simulation results give insights into the complexity of the coupling of the different phenomena controlling the dynamics of the studied system. For instance, the results show that for values of the capillary number much smaller than unity, that is, for spherical bubbles, the bubble velocity decreases as the bubble diameter increases. Moreover, surfactants tend to decrease significantly the bubble velocity, when compared with a bubble with a clean surface. Indeed, they accumulate at a convergent stagnation point/circle on the bubble surface and deplete at a divergent stagnation point/circle. As a consequence, the velocity of the liquid adjacent to the bubble is reduced in between the convergent and divergent stagnation points/circles because of Marangoni stresses. It is shown that regarding the bubble–liquid relative velocity, the bubble behaves as a rigid sphere when the Langmuir number is larger than unity, at least for the range of parameters explored in this study. For values of the capillary number of the order of unity, the bubble can take a "bullet shape". In this case, the bubble velocity increases as the bubble diameter increases. This increase of the bubble–liquid relative velocity is linked to a drastic change in the liquid flow structure near the bubble. Surfactants are swept to the rear of the bubble and have less influence on the bubble dynamics than for spherical bubbles. Finally, it is shown that increasing the amount of surfactants adsorbing to the surface eventually leads to the bursting of the bubble.

INTRODUCTION

Investigation of microscale flows is relevant for many microfluidic applications such as microheat exchangers, microabsorbers, and microextractors.[1,2] In recent years, bubble microabsorbers were developed for industrial applications, and consequently, the motion of bubbles in microchannels was investigated thoroughly. In such a gas–liquid microscale flow, inertial effects are often negligible while surface tension and viscous forces dominate the system. The relative importance of inertial to viscous forces is assessed by the means of the Reynolds number: $Re = \rho J_l d/\mu$, where ρ, μ, J_l and d are the density and viscosity of the liquid, the mean flow velocity, and the bubble diameter, respectively. The Reynolds number characterizing these microscale flows is often close or smaller than unity. The relative importance of viscous forces to surface tension forces is assessed by the means of the capillary number: $Ca = J_l\mu/\sigma$, where σ is the surface tension of the gas–liquid interface.

Among the investigations regarding the motion of bubbles in microchannels, the dynamics of bubbles with a volume equivalent diameter, d, larger than the channel equivalent diameter, d_h, has received considerable attention.[3−7] The

bubble equivalent diameter is defined as $d = (6V/\pi)^{1/3}$, where V is the bubble volume. For example, it was shown that the mass transfer in those systems is considerably enhanced due to recirculation of the liquid in between bubbles, promoting mixing.[3] On the other hand, the motion and dissolution of small bubbles in microchannels, that is, bubbles with $d/d_h < 1$, has received less attention. Cubaud et al. (2012) studied experimentally and globally the dissolution of spherical bubbles within microchannels.[8] Feng (2010) studied the effect of Re and Ca on the dynamics of an isolated small bubble in a horizontal channel.[9] Khodaparast et al. (2015) studied, with experiments and numerical simulations, the motion of bubbles inside horizontal channels.[10] In their work, Re and Ca were varied (in the ranges $10^{-3} < Re < 10^{3}$ and $10^{-4} < Ca < 10^{-1}$) and the shape and the velocity of the bubble, V_b, was monitored. For $d/d_h < 1$, they observed that V_b/J_l decreases as d/d_h is increased. The same behavior was observed by Kurimoto et al. (2013) for buoyancy driven bubbles in vertical pipes.[11] Stan et al. (2011) studied the influence of Archimedes' thrust on the vertical position of spherical bubbles within a horizontal and straight rectangular microchannel.[12] They also observed that, for neutrally buoyant bubbles characterized by small Re and moderate Ca, the equilibrium position of the bubble is near the symmetry axis of the channel. At larger Re, they observed that inertial migration forces shift this position off the horizontal symmetry plane of the channel.

When surfactants are introduced in the liquid, they may adsorb on the bubble surface and alter the surface tension of the gas−liquid interface. Consequently, an inhomogeneous distribution of the surfactants on the interface causes Marangoni stresses, influencing the dynamics of the bubble.[13−17] This property of surfactants make them widely used in microfluidics to stabilize emulsions or to favor the formation of bubbles or droplets.[18,19] Regarding the dynamics of small bubbles translating along microchannels, Mikaelian et al. (2015) performed direct numerical simulations of spherical bubbles, that is, for $Ca \to 0$, translating along a horizontal channel.[20] They investigated the effect of bubble confinement, through varying the parameter d/d_h, on the bubble velocity. They considered two limiting situations to model the presence of surfactants. They imposed a zero shear stress on the gas−liquid interface to model the case of a clean interface. The presence of surfactants was accounted for by imposing a no slip condition on the gas−liquid interface (i.e., by imposing that the bubble behaves as a rigid sphere). They established correlations to calculate the ratio of the bubble velocity to the mean flow velocity, V_b/J_l, as a function of d/d_h, for the case of a clean interface

$$\frac{V_b}{J_l} = 1 + \exp\left(-1.83\left(\frac{d}{d_h}\right)^5\right) \tag{1}$$

and for a bubble behaving as a rigid sphere

$$\frac{V_b}{J_l} = 1 + \exp\left(-1.92\left(\frac{d}{d_h}\right)^{9/4}\right) \tag{2}$$

These correlations were established in the range $0.15 \le d/d_h \le 0.75$. Note that Rivero Rodriguez and Scheid (2018) extended the explored numerical range to $0 < d/d_h \le 0.9$ and used polynomial fittings to express V_b/J_l as a function of d/d_h.[21]

The effect of the surfactants on the velocity of the liquid adjacent to the bubble surface depends on their distribution on the gas−liquid interface. This distribution can be determined by solving the complete set of coupled partial differential equations governing the transport of surfactants on the bubble surface and in the liquid. In a microchannel bubbly flow, because of the bubble confinement created by the channel walls, the distribution of surfactants on the gas−liquid interface is expected to be fundamentally different from their distribution in the case of a bubble rising in an infinite liquid medium. To the best of our knowledge, the distribution of surfactants on the surface of a small bubble (i.e., $d/d_h < 1$) translating in a horizontal microchannel has not been studied yet. Furthermore, the effect of the bubble deformability (i.e., the effect of Ca) on V_b/J_l in the presence of surfactants has not been studied in previous works.

Accordingly, in this study, we investigate, by direct numerical simulations, the combined effect of the bubble deformability, the presence of surfactants, and the bubble confinement on the dynamics of small bubbles (i.e., $d/d_h < 1$) transported by a liquid in a horizontal microchannel. We consider the presence of surfactants by simulating their transport on the surface of the bubble and inside the liquid phase. We compute the Marangoni stress induced by their inhomogeneous distribution on the surface. The numerical code used for this study is the JADIM code, which has been developed to simulate dispersed two phase flows.[14,22−25] Our analysis emphasizes on several parameters characterizing the system: the bubble shape, the ratio of the bubble velocity to the mean flow velocity, V_b/J_l, the drag coefficient of the bubble, C_d, the fluid velocity tangent to the bubble surface, V_s/V_b, and the surfactant distribution on the interface, Γ. Our goal is to highlight and quantify the key phenomena governing the studied system.

PROBLEM STATEMENT

Geometry. We consider an axisymmetric bubble of diameter d moving in a horizontal and rectilinear microchannel with a circular cross section (referred to as a cylindrical microchannel in this work) of diameter d_h, as sketched in Figure 1. The channel has a length L and a pressure difference $\Delta p > 0$ is imposed between the left and the right boundaries of the domain. The bubble is centered in the channel. Rivero Rodriguez and Scheid (2018) have recently shown that centered bubbles are stable provided that d/d_h is larger than 0.85 or that the Ohnesorge number $Oh = \sqrt{Ca/\mathrm{Re}}$ is larger or

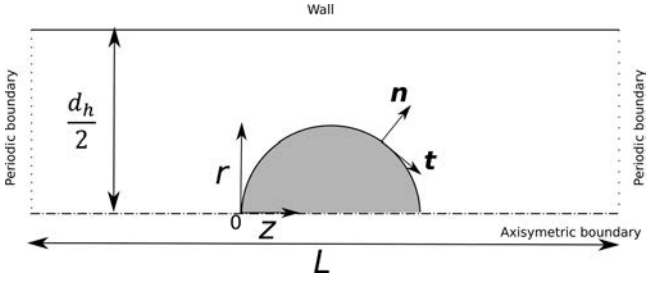

Figure 1. Axisymmetric bubble of density ρ_d and viscosity μ_d immersed in a viscous liquid of density ρ_c and viscosity μ_c inside a cylindrical microchannel of length L and diameter d_h. The unit vector normal to the gas−liquid interface, $\boldsymbol{n}$, and the unit vector tangent to the gas−liquid interface, $\boldsymbol{t}$, are sketched in this figure.

equal to 0.2 for bubbles with $d/d_h < 0.85$. In addition, they showed that regardless of the value of Oh, V_b/J_I and the bubble shape are not affected by Re provided that $Re \lesssim 8$. In this study, a particular attention is held to ensure that $Oh \geq 0.2$, so that the bubble can be considered as centered. The liquid and the bubble surface contain surfactants with initial concentrations C_∞ and Γ_0, respectively.

Equations and Modeling Assumptions. Under the assumptions that (i) the fluids are Newtonian and incompressible, (ii) there is no gas−liquid mass transfer through the interface, and (iii) the flow is isothermal, the velocity field $\boldsymbol{v}$ and the pressure p satisfy the classical one fluid formulation of the Navier−Stokes equations:[26]

$$\nabla\cdot\boldsymbol{v} = 0 \tag{3}$$

$$\frac{\partial \boldsymbol{v}}{\partial t} + \boldsymbol{v}\cdot\nabla\boldsymbol{v} = -\frac{1}{\rho}\nabla p + \frac{1}{\rho}\nabla\cdot\bar{\boldsymbol{T}} - \frac{\sigma}{\rho}(\nabla\cdot\boldsymbol{n})\boldsymbol{n}\delta_I - \frac{1}{\rho}\nabla\sigma\delta_I \tag{4}$$

where $\boldsymbol{T} = \mu(\nabla\boldsymbol{v} + (\nabla\boldsymbol{v})^T)$ is the viscous stress tensor, ρ, μ, σ are the density, dynamic viscosity, and surface tension, respectively, $\boldsymbol{n}$ is a unit vector normal to the interface, arbitrarily chosen pointing toward the liquid phase (see Figure 1), and δ_I is the Dirac distribution associated with the bubble−liquid interface.

The transport equations of the surfactants in the liquid phase and on the gas−liquid interface are given by[14,27]

$$\frac{\partial C}{\partial t} + \boldsymbol{v}_c\cdot\nabla C = \nabla\cdot(D_c\nabla C) \tag{5}$$

$$\frac{\partial \Gamma}{\partial t} + \nabla_s\cdot(\boldsymbol{v}_s\Gamma) = D_s\nabla_s^2\Gamma + S_\Gamma \tag{6}$$

where C is the surfactant concentration in the liquid phase, Γ is the surfactant concentration on the gas−liquid interface, D_c and D_s are the diffusion coefficients of the surfactants in the liquid phase and along the interface, respectively, $\boldsymbol{v}_c$ is the velocity field in the liquid phase, $\boldsymbol{v}_s$ is the projection of $\boldsymbol{v}_c$ on the tangent to the interface, $\nabla_s = ((\mathbf{I} - (\boldsymbol{n}\otimes\boldsymbol{n}))\cdot\nabla)$ is the surface gradient operator,[28] and S_Γ is the flux of surfactants from the liquid phase to the interface because of the adsorption/desorption of the surfactants, i.e., $S_\Gamma = (D_c\boldsymbol{n}\cdot\nabla C)|_I$, where the subscript I denotes the bubble−liquid interface. It is given by[14,29]

$$S_\Gamma = k_a C_I(\Gamma_\infty - \Gamma) - k_d\Gamma \tag{7}$$

where k_a and k_d are adsorption and desorption kinetic constants, respectively, and C_I is the surfactant concentration in the liquid in contact with the interface.

It is assumed that the surface tension depends on the surfactant concentration on the interface according to an equation of state derived from the Langmuir adsorption isotherm[30]

$$\sigma = \sigma_0 + RT\Gamma_\infty \ln\left(1 - \frac{\Gamma}{\Gamma_\infty}\right) \tag{8}$$

where R is the ideal gas constant, T is the absolute temperature, σ_0 is the surface tension of the clean interface, and Γ_∞ is the maximum packing concentration of surfactants on the interface.

Considering the boundary conditions, periodicity is imposed between the inlet and the outlet of the domain, simulating therefore a train of bubbles, a no slip condition with zero transfer rate is imposed on the wall and a symmetry condition is imposed on the symmetry axis:

$$\begin{cases} \boldsymbol{v}|_{z_{left}} = \boldsymbol{v}|_{z_{right}} \\ \boldsymbol{v}|_{r=d_h/2} = 0 \\ \boldsymbol{v}\cdot\boldsymbol{n}_a|_{r=0} = 0 \end{cases} \tag{9}$$

$$\begin{cases} C|_{z_{left}} = C|_{z_{right}} \\ \nabla C\cdot\boldsymbol{n}_w|_{r=d_h/2} = 0 \\ \nabla C\cdot n_a|_{r=0} = 0 \end{cases} \tag{10}$$

$$\begin{cases} \Gamma|_{z_{left}} = \Gamma|_{z_{right}} \\ \nabla\Gamma\cdot\boldsymbol{n}_a|_{r=0} = 0 \end{cases} \tag{11}$$

$$\{p|_{z_{left}} = p|_{z_{right}} + \Delta p \tag{12}$$

where $\boldsymbol{n}_w$ is the unit vector normal to the channel wall, $\boldsymbol{n}_a$ is the unit vector normal to the symmetry axis, (z,r) are the axial and radial coordinates, respectively (see Figure 1), and z_{left} and z_{right} are the axial coordinates localizing the left and right boundaries of the computational domain, respectively.

Dimensional Analysis. The governing equations are solved in their dimensional forms and the results are expressed in terms of relevant dimensionless parameters. Let $\mathcal{L}$ and $\mathcal{U}$ be appropriately defined length and velocity scales, respectively. The number of dimensional parameters, 16, minus the number of dimensions, 4, results in 12 dimensionless numbers allowing the characterization of the problem. Two of them characterize the geometry of the system, whereas 10 others characterize its dynamics. These 10 dimensionless numbers are defined as follows

$$\begin{aligned} &Re = \frac{\rho_c\mathcal{U}\mathcal{L}}{\mu_c},\ Ca = \frac{\mu_c\mathcal{U}}{\sigma_0},\ m = \frac{\rho_d}{\rho_c},\ \lambda = \frac{\mu_d}{\mu_c} \\ &E = \frac{RT\Gamma_\infty}{\sigma_0},\ La = \frac{k_aC_\infty}{k_d},\ Da = \frac{\Gamma_\infty}{\mathcal{L}C_\infty},\ \alpha = \frac{k_aC_\infty\mathcal{L}}{\mathcal{U}}, \\ &Pe = \frac{\mathcal{U}\mathcal{L}}{D_c},\ Pe_s = \frac{\mathcal{U}\mathcal{L}}{D_s} \end{aligned} \tag{13}$$

where Re, Ca, E, La, Da, α, Pe, Pe_s, m, and λ are the Reynolds number, capillary number, elasticity number, Langmuir number, Damkohler number, dimensionless adsorption rate, Peclet number based on the bulk surfactant diffusivity, Peclet number based on the interfacial surfactant diffusivity, ratio of the gas viscosity (μ_d) to the liquid viscosity (μ_c), and ratio of the gas density (ρ_d) to the liquid density (ρ_c), respectively.

The velocity scale $\mathcal{U}$ is set equal to the mean velocity of the monophasic liquid Poiseuille flow that would have been generated by the imposed pressure gradient, $\Delta p/L$: $\mathcal{U} = J_{lref} = \Delta p d_h^2/(32\mu_c L)$, and the length scale is set as $\mathcal{L} = d$. This length scale sets the two dimensionless numbers characterizing the geometry: d/d_h and L/d. It has been verified that the difference between J_{lref} and the actual value of J_l obtained in the simulations varies between 0.8 and 2.8%, confirming that the chosen scale is appropriate for the setup considered in this work. The capillary number, Langmuir number, and ratio of the bubble equivalent diameter to the tube diameter are varied in the range $10^{-2} < Ca < 1$, $0 < La < 10$, and $0.15 < d/d_h < 0.75$, respectively. The other parameters

are set to values usually encountered for surfactants in bubbly flows: $Da = 0.1$, $E = 0.12$, $\alpha = 0.1$, $Pe_s = \infty$.[16,31] Furthermore, the parameters m and λ are set to $m = 10^{-3}$ and $\lambda = 10^{-2}$, which are typical values encountered in bubbly flows. To satisfy the criterion $\sqrt{Ca/\mathrm{Re}} \geq 0.2$, the value of Re is either set equal to 1 if $Ca \geq 0.04$ or to $Ca/0.04$ if $Ca < 0.04$. As discussed earlier, the bubble shape and V_b/J_l do not depend on Re for $Re \lesssim 8$. The value of Pe sets the thickness of the surfactant diffusion boundary layer around the bubble. A particular attention has to be paid to capture the surfactant concentration gradients within this boundary layer. As a consequence, the value of Pe is set to a moderate value, $Pe = 500$, to avoid too large computational costs. The value of L/d is increased gradually, starting from 4, until V_b/J_l becomes independent of L/d.

NUMERICAL PROCEDURE

The numerical code used for this study is the JADIM code developed to perform local analyses of dispersed two phase flows. To study the dynamics of a small bubble in a microchannel in the presence of surfactants, we have introduced the resolution of the surfactant transport equation on the gas−liquid interface and in the liquid in the level set (LS) modulus of JADIM.[23,32] The distribution on the interface of the Marangoni stress induced by the inhomogeneous distribution of the surfactants on the gas−liquid interface is computed using the continuum surface force (CSF) model. In JADIM, the implemented LS method consists in an Eulerian description of each phase on a fixed grid, the interface between the two phases being calculated using the transport equation of the signed distance function to the interface, ϕ. The two fluids are assumed to be Newtonian and incompressible, with no phase change.

Level-Set Method. The location of each phase with respect to the interface is given by the signed distance function to the interface (or LS function), $\phi(\mathbf{x},t)$. This distance function obeys to the following transport equation[33]

$$\frac{\partial \phi}{\partial t} + \boldsymbol{v}\cdot\nabla\phi = 0 \tag{14}$$

ϕ is defined as being positive in the gas phase and negative in the liquid phase. A classical redistanciation equation is applied to the LS function at each time step

$$\frac{\partial \phi}{\partial \tau} + \mathrm{sign}(\phi)(|\nabla\phi| - 1) = 0 \tag{15}$$

where τ is a fictitious time. The sign function is[34]

$$\mathrm{sign}(\phi(\mathbf{x}, t)) = \frac{\phi}{\sqrt{\phi^2 + \Delta x^2}} \tag{16}$$

where Δx is the grid size.

The normal to the interface, $\boldsymbol{n}$, and the interface curvature, κ, are computed with the LS function as follows:

$$\boldsymbol{n} = -\frac{\nabla\phi}{||\nabla\phi||} \tag{17}$$

and

$$\kappa = -\nabla\cdot\left(\frac{\nabla\phi}{||\nabla\phi||}\right) \tag{18}$$

The tangent to the interface, $\boldsymbol{t}$ (see Figure 1), is calculated as $\boldsymbol{t} = -\frac{1}{||\nabla\phi||}\left(\frac{\partial\phi}{\partial r}, -\frac{\partial\phi}{\partial z}\right)$. The volume fraction of the gas phase in a given computational cell, F, is computed from the LS function using a smooth Heaviside function

$$F = H(\phi) = \begin{cases} 0 & \text{if } \phi(x) < -\epsilon \\ \frac{1}{2}\left(1 + \frac{\phi}{\epsilon} + \frac{1}{\pi}\sin\left(\frac{\pi\phi}{\epsilon}\right)\right) & \text{if } -\epsilon < \phi(x) < \epsilon \\ 1 & \text{if } \phi(x) > \epsilon \end{cases} \tag{19}$$

where $\epsilon = \sqrt{2}\Delta x$ is the half numerical thickness of the interface. The local viscosity and density, μ and ρ, are calculated using an arithmetic mean of the properties of each phase: $\mu = \mu_c(1 - F) + \mu_d F$, $\rho = \rho_c(1 - F) + \rho_d F$.

Transport of the Surfactants in the Bulk of the Liquid and on the Gas−Liquid Interface. In an Eulerian description of each phase on a fixed grid and for incompressible fluids, the following equivalent form of eq 6 is used[34−36]

$$\frac{\partial \tilde{\Gamma}}{\partial t} + \boldsymbol{v}\cdot\nabla\tilde{\Gamma} - \tilde{\Gamma}\boldsymbol{n}\cdot(\nabla\boldsymbol{v})\cdot\boldsymbol{n} = D_s[\nabla^2\tilde{\Gamma} - \kappa\nabla\tilde{\Gamma}\cdot\boldsymbol{n} - \boldsymbol{n}\cdot\mathbf{D}^2\tilde{\Gamma}\cdot\boldsymbol{n}] + S_{\tilde{\Gamma}} \tag{20}$$

where $\mathbf{D}^2\tilde{\Gamma}$ is the Hessian matrix of $\tilde{\Gamma}$, $S_\Gamma = k_a C_l(\Gamma_\infty - \tilde{\Gamma}) - k_d\tilde{\Gamma}$ and $\tilde{\Gamma}$ is a scalar field defined on the whole computational domain; $\tilde{\Gamma}$ is the result of the extrapolation of Γ from the interface toward the liquid and gas phases. Accordingly, the following partial differential equation (PDE) is solved after each physical time step of the procedure, with the initial condition $\tilde{\Gamma}^*(\mathbf{x},\tau = 0) = \tilde{\Gamma}(\mathbf{x},t)$[34]

$$\frac{\partial \tilde{\Gamma}^*}{\partial \tau} + \mathrm{sign}(\phi)\frac{\nabla\phi}{||\nabla\phi||}\cdot\nabla\tilde{\Gamma}^* = 0 \tag{21}$$

This method allows calculating the time evolution of Γ, a quantity associated with a moving and deforming surface, in a fixed coordinate system.[34] As pointed out by Xu and Zhao (2003), it has been observed that five iterations are sufficient when solving eq 21, for $\tilde{\Gamma}^*$ to reach its converged values with respect to τ. Indeed, we have checked that the relative variation of the values of $\tilde{\Gamma}^*$ is less than 0.5% when the number of fictitious time step is increased from 4 to 8.

Following Muradoglu and Trigvason (2008) and Hayashi and Tomiyama (2012), eq 5 is solved under a no flux boundary condition at the interface: $(D_c\boldsymbol{n}\cdot\nabla C)|_I = 0$. Consequently, the boundary condition of eq 5, $S_\Gamma = (D_c\boldsymbol{n}\cdot\nabla C)|_I$, is included in the bulk transport equation as an interfacial source term $S_\Gamma\delta_I$

$$\frac{\partial C}{\partial t} + \boldsymbol{v}\cdot\nabla C = \nabla\cdot(D_c\nabla C) - S_{\tilde{\Gamma}}\delta_I \tag{22}$$

In this technique, an implicit assumption is made that all of the surfactant transfer from the liquid phase to the gas−liquid interface takes place in a thin layer adjacent to the interface. In other words, the total amount of surfactants adsorbed from the liquid to the interface is distributed along this thin layer and added as an interfacial source term in the transport equation. The no flux condition is enforced by extrapolating C from the interface to the gas phase, solving the following PDE at each physical time step, with the initial condition $C^*(\mathbf{x},\tau = 0) = C(\mathbf{x},t)$

$$\frac{\partial C^*}{\partial \tau} + \mathrm{sign}(\phi)\frac{\nabla \phi}{||\nabla \phi||}\cdot\nabla C^* = 0 \tag{23}$$

In this study, eq 23 was solved performing five fictitious time step. It has been verified that the computed values of C^* are not modified by more than 0.5% if more iterations are performed. The time scheme used for solving eqs 14, 15, and 20−23 is a third order Runge−Kutta scheme. The spatial scheme used for the advective terms in the different equations is the conservative form of the fifth order WENO scheme, whereas a second order centered scheme is used for the other terms.

Equation 8 is slightly modified to avoid negative values of the surface tension[15] and is rewritten in terms of $\tilde{\Gamma}$

$$\sigma = \sigma_0\left\{\max\left[\epsilon_0,\ 1 + \frac{RT\Gamma_\infty}{\sigma_0}\ln\left(1 - \frac{\tilde{\Gamma}}{\Gamma_\infty}\right)\right]\right\} \tag{24}$$

where $\epsilon_0 = 0.05$. Equation 24 is representative of the variation of the surface tension of an interface with its surfactant concentration. For instance, in the case of stretching liquid bridges, it was shown that σ reaches a plateau when Γ approaches Γ_∞.[37]

Navier−Stokes Equations Solver. The system of eqs 3 and 4 is discretized on a staggered grid using a finite volume method. All spatial derivatives are discretized using second order centered schemes. The time scheme used to compute the advective terms in the Navier−Stokes equations is a third order Runge−Kutta scheme, whereas the viscous stresses are computed using a semi implicit Crank−Nicolson method. The incompressibility is ensured using a projection method. Further details on the numerical algorithms concerning the spatial discretization, as well as the time advancement procedure, can be found in Magnaudet el al. (1995) or in Legendre and Magnaudet (1998).[24,38]

The CSF model is used to compute the capillary term in eq 3[39]

$$\frac{\sigma}{\rho}(\nabla\cdot\boldsymbol{n})\boldsymbol{n}\delta_I \approx \frac{-\overline{\sigma}}{\rho V}\nabla F\int_s \frac{\nabla\phi}{||\nabla\phi||}\cdot\boldsymbol{n}_{\mathrm{cell}}\,\mathrm{d}S \tag{25}$$

where $\boldsymbol{n}_{\mathrm{cell}}$ is the unit vector normal to the faces of the cells centered on the velocity points, σ is the local value of σ at the center of these cells, $\mathrm{d}S$ is the area of the cell faces, and s denotes a surface integral. The Marangoni stress is also computed at the center of the cells centered on the velocity points

$$\frac{1}{\rho}\nabla_s\sigma\delta_I = \left[\nabla\sigma - \frac{\nabla\phi}{||\nabla\phi||}\left(\frac{\nabla\phi}{||\nabla\phi||}\cdot\nabla\sigma\right)\right]\left(\frac{2\rho}{\rho_c + \rho_d}\right)\delta(\phi)_I \tag{26}$$

where $\delta(\phi)_I$ is a smoothed Dirac function, which allows spreading the effect of the Marangoni stress over the numerical thickness of the interface

$$\begin{cases}\delta(\phi)_I = \dfrac{1}{2\epsilon}\left[1 + \cos\left(\dfrac{\pi\phi}{\epsilon}\right)\right], & \text{for } |\phi| < \epsilon\\ \delta(\phi)_I = 0 \text{ otherwise}\end{cases} \tag{27}$$

Grid. A uniform grid with square cells is used for the computations. At least four cells are placed inside the concentration boundary layers. The thickness of the boundary layers on the channel wall and on the gas−liquid interface (δ_w and δ_b) are estimated as $\delta_b \approx d/\sqrt{Pe}$ and $\delta_w \approx d_h/\sqrt{Pe}$. The dimensions of the square cells are deduced such that at least four cells are placed in the concentration boundary layer around the bubble: $\Delta z = \Delta r = d/(4\sqrt{Pe})$.

VALIDATION OF THE NUMERICAL PROCEDURE

The LS modulus of JADIM has been validated previously.[5,23] Specific validation tests regarding surfactant induced Marangoni stress have been performed and are reported in the Supporting Information. Those tests aim to validate the numerical implementation of (i) the different terms in the equation describing the surfactant transport on the gas−liquid interface, (ii) the source/sink term in the equation describing the exchanges of surfactants between the bulk and the interface, and (iii) the computation of the Marangoni stress. Namely those tests include

1. (i) A surface expansion test where the implementation of the term $\tilde{\Gamma}\boldsymbol{n}\cdot\nabla\boldsymbol{v}\cdot\boldsymbol{v}$ in eq 20 is validated,
2. (i) A surface advection test where the implementation of the term $\boldsymbol{v}\cdot\nabla\tilde{\Gamma}$ in eq 20 is validated,
3. (i) A surface adsorption test where the implementation of the term $(k_aC_I(\Gamma_\infty - \tilde{\Gamma}) - k_d\tilde{\Gamma})\delta_I$ in eq 20 is validated,
4. (i) A diffusion test where the implementation of the term $D_s[\nabla^2\tilde{\Gamma} - \kappa\nabla\tilde{\Gamma}\cdot\boldsymbol{n} - \boldsymbol{n}\cdot\mathbf{D}^2\tilde{\Gamma}\cdot\boldsymbol{n}]$ in eq 20 is validated,
5. (ii) A bulk exchange test where the implementation of the term $(k_aC_I(\Gamma_\infty - \tilde{\Gamma}) - k_d\tilde{\Gamma})\delta_I$ in eq 22 is validated,
6. (iii) A test to validate the computation of the Marangoni stress, that is, $\nabla_s\sigma$ in eq 3.

For each test case (i, ii, and iii), the convergence of the simulation is investigated. As a result, the overall convergence order of the solver is third order in time and near second order in space. All these tests are available in the Supporting Information. In this section, the validation of the whole numerical procedure is done using a rising bubble as a test case.

A bubble is initialized at the center of an axisymmetric domain. The domain and the boundary conditions are the same as those introduced in Figure 1, with $L/d = 20$, $d_h/d = 16$, and $\Delta p/L = \rho_c g$, where g is the gravity acceleration (i.e., gravity acts along the negative z axis (see Figure 1) and, consequently, the bubble rises due to its density difference with the surrounding liquid). The bubble interface is initially clean, that is, $\tilde{\Gamma}(\mathbf{x},t = 0) = 0$. The surfactant concentration is initially uniform in the liquid $C(\mathbf{x},t = 0) = C_\infty$. The problem is governed by the following dimensionless numbers: E, La, Da, α, Pe, Pe_s, ρ_d/ρ_c, μ_d/μ_c, Eo, and Mo, where $Eo = ((\rho_c - \rho_d)gd^2)/\sigma$ is the Eotvos number and $Mo = ((\rho_c - \rho_d)g\mu_c^4)/(\rho_c^2\sigma^3)$ is the Morton number. The parameters are fixed to $E = 0.5$, $Da = 10$, $\alpha = 20$, $Pe = 10$, $Pe_s = 100$, $m = 0.1$, $\lambda = 0.025$, $Eo = 1$, $Mo = 0.1$, and La is set to 0 or 1. The terminal bubble velocity computed with JADIM is compared with values computed by Tasoglu et al. (2008), who solved the same problem using a finite difference/front tracking method.[15] For the chosen parameters, a clean buoyant bubble is spherical.[40] The terminal values of the bubble Reynolds number, $Re_b = \rho_c V_b d/\mu_c$, obtained by Tasoglu et al. (2008) for a clean bubble ($La = 0$) and a contaminated one ($La = 1$) are summarized in Table 1 together with the values obtained using JADIM. As it can be seen in Table 1, the values computed with JADIM are in excellent agreement with those computed by Tasoglu et al.

Table 1. Comparison between the Values of the bubble Terminal Reynolds Number, Re_b, Obtained in This Study and the Ones Obtained by Tasoglu et al. (2008)

La	0	1
Tasoglu et al. (2008)	0.241	0.164
present study	0.239	0.161

(2008). The convergence rate of Re_b with respect to the mesh size for $La = 1$ was determined to be about 1.5.

Simulations were also performed varying Eo, Mo, and La. The drag force acting on the bubble, F_d, has been computed using the cylindrical coordinate system (r,z) as follows

$$F_d = 2\pi \int_{z_r}^{z_f} (\tau_{nt}(z, r_l(z)) - (-p_c(z, r_l(z)) + \tau_{nn}(z, r_l(z)))r_l'(z))r_l(z)\, dz \tag{28}$$

where z_r and z_f are the axial coordinates localizing the back and the front of the bubble, respectively, $r_l(z)$ is the radial coordinate localizing the gas–liquid interface, $r_l' = \frac{dr_l}{dz}$, $\tau_{nt} = (\boldsymbol{T}\cdot\boldsymbol{n})\cdot\boldsymbol{t}$ is the tangent viscous stress, $\tau_{nn} = (\boldsymbol{T}\cdot\boldsymbol{n})\cdot\boldsymbol{n}$ is the normal viscous stress, and p_c is the periodic component of the pressure inside the liquid (i.e., $p_c = p + \Delta p/Lz$). To evaluate F_d, the values of τ_{nt} and τ_{nn} are first calculated at the center of the computational cells and then interpolated on the gas–liquid interface.

The drag coefficient of the spherical bubble, based on the terminal bubble velocity and its diameter, is then computed for each simulation: $C_d = F_d/(0.5\rho_c\pi(d/2)^2 V_b^2)$. In Figure 2, drag

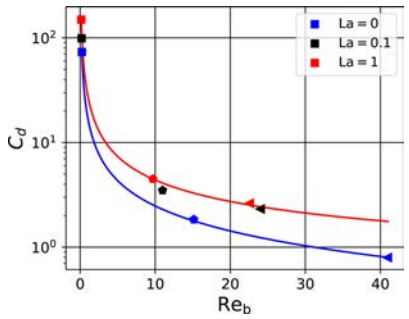

Figure 2. Drag coefficient, C_d, of a buoyant bubble as a function of its Reynolds number (terminal value). Squares, pentagons, and triangles are values of the drag coefficient of the bubble computed with JADIM for values of the Eotvos number and Morton number equal to (Eo = 1; Mo = 0.1), (Eo = 1; $Mo = 10^{-5}$), and (Eo = 0.1; $Mo = 10^{-9}$), respectively. Blue, black, and red symbols are values corresponding to La = 0, La = 0.1, and La = 1, respectively. The red and blue solid lines give values of the drag coefficient predicted by the correlations given in eqs 30 and 29, respectively.

coefficients computed with JADIM are compared with correlations predicting C_d as a function of Re_b for a clean bubble[41]

$$C_d = \frac{24}{Re_b}\left(\frac{2}{3} + \left(\frac{12}{Re_b} + 0.75\left(1 + \frac{3.315}{Re_b^{1/2}}\right)\right)^{-1}\right) \tag{29}$$

and for a rigid sphere[42]

$$C_d = \frac{24}{Re_b}(1 + 0.15Re_b^{0.687}) \tag{30}$$

It can be observed in Figure 2 that varying La from 0 to 1 allows obtaining a bubble rising with a drag coefficient characterizing a bubble with a clean interface (for La = 0) or characterizing a rigid sphere (for La = 1).

RESULTS

In this section, the dynamics of a small bubble inside a horizontal microchannel is studied. Initially, that is, at t = 0 s, the bubble is at the center of the computational domain, as sketched in Figure 1. The liquid surrounding the bubble contains surfactants with an initially homogeneous concen tration, C_∞. The independency of the bubble terminal velocity on the initial surfactant concentration on the bubble–liquid interface, Γ_0, has been verified. To illustrate this statement, the instantaneous bubble velocity, V_b, is presented in Figure 3 as a

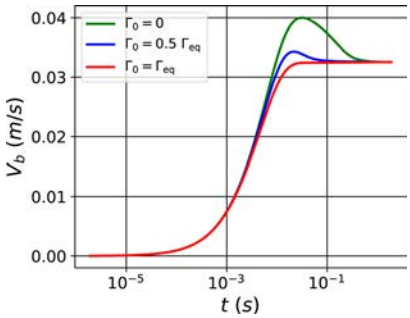

Figure 3. V_b as a function of the time for different values of the initial concentration of surfactants on the gas–liquid interface: $\Gamma_0 = 0$, $\Gamma_0 = 1/2\Gamma_{eq}$, and $\Gamma_0 = \Gamma_{eq}$, for Ca = 0.01, d/d_h = 0.75, and Re = 0.25.

function of the time t, for different values of Γ_0, as compared to the equilibrium value $\Gamma_{eq} = \Gamma_\infty La/(1 + La)$. For $\Gamma_0 = 0$, it can be observed that the bubble first accelerates. Then, as surfactants adsorb on the bubble–liquid interface, V_b begins to decrease until it reaches its terminal value. When Γ_0 is increased, the bubble reaches its terminal velocity at an earlier time. It is observed that this terminal velocity is not affected by the value of Γ_0. Therefore, in all of the numerical simulations presented in this work, the initial concentration of surfactants on the bubble–liquid interface is set to the equilibrium value: $\Gamma_0 = \Gamma_{eq}$. In this way, the effective simulation time is reduced.

The mass of surfactants is monitored on the bubble surface as $M(t) = \int_{S(t)} \tilde{\Gamma}\, dS(t)$, following the method of Xu and Zhao (2002). The simulations are stopped when the relative variation of $M(t)$ and of the bubble velocity, V_b, is less than 1%. Unless explicitly mentioned, all of the results presented in this section relate to a stationary state of the studied system.

In the first part of this section, the dynamics of a small spherical bubble, that is, $Ca \ll 1$, inside a horizontal microchannel is studied. The second part deals with the shape and the flow field around a deformable bubble, in the absence of surfactants. Finally, the combined effect of surfactants and bubble deformability on the bubble dynamics is analyzed.

Spherical Bubbles. Figure 4 presents the steady state surface concentration field of the surfactants, $\tilde{\Gamma}$ (presented at the vicinity of the bubble surface only), bulk concentration field of the surfactants, C, and velocity streamlines in a reference frame attached to the bubble mass center, for Re = 0.25, $Ca = 10^{-2}$, d/d_h = 0.75, La = 0 (Figure 4a), La = 0.1

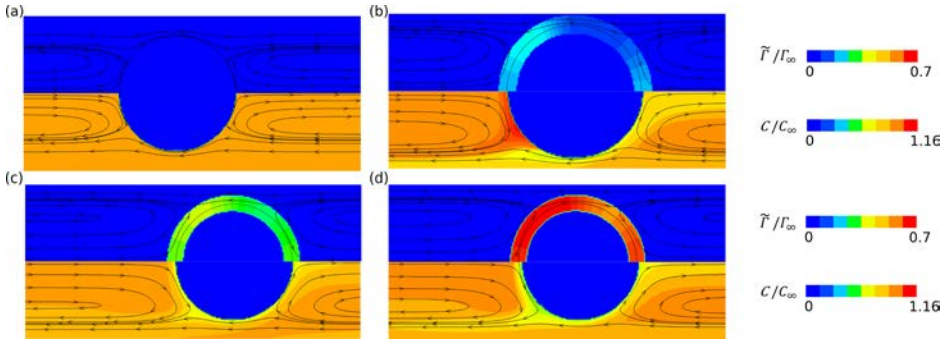

Figure 4. Contour plots of (top) the surfactant concentration field on the bubble surface, $\tilde{\Gamma}$, and (bottom) the bulk surfactant concentration field, C. Velocity streamlines are drawn in a reference frame translating with the bubble. The bubble moves from the left to the right. (a) $La = 0$, (b) $La = 0.1$, (c) $La = 1$, and (d) $La = 10$.

(Figure 4b), $La = 1$ (Figure 4c), and $La = 10$ (Figure 4d). The bubble moves from the left to the right in a laboratory reference frame. As expected, for $Ca = 10^{-2}$ and for $Re \approx 1$, the bubble is spherical. As it can be observed in Figure 4, the structure of the liquid flow in the microchannel appears to differ significantly from the one observed when a bubble rise in a liquid of infinite extend. More specifically, it is observed that the flow structure generates a convergent stagnation point at the front of the bubble (point A in Figure 5) and a divergent

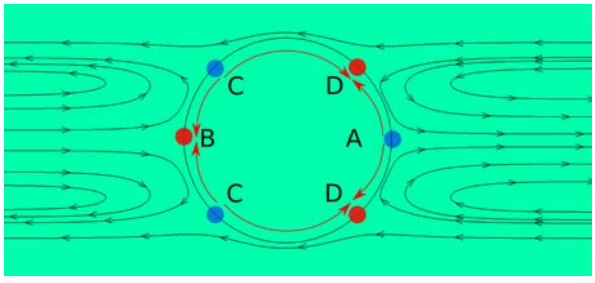

Figure 5. Spherical bubble inside a microchannel. The bubble goes from left to right. Red dots depict a divergent stagnation point/circle on the bubble surface, where consequently the surface tension is high. Green dots depict a convergent stagnation point/circle on the bubble surface where the surface tension is low. Velocity vectors, in black, are drawn in a reference frame attached to the bubble mass center. Red arrows depict the direction of the Marangoni stress.

stagnation point at the rear of the bubble (point B in Figure 5). Moreover, the flow generates a convergent stagnation circle on the back half of the bubble side (C in Figure 5) and a divergent stagnation circle on the front half of the bubble side (D in Figure 5). Consequently, on the surface, the surfactants accumulate near the convergent point/circle and are depleted near the divergent point/circle. This is clearly observed in Figure 4.

The surfactants reduce the surface tension and, consequently, their inhomogeneous distribution on the bubble–liquid interface induces surface tension gradients that are expected to alter the fluid velocity along the interface. In Figure 6a–d, the dimensionless surfactant concentration on the bubble surface, $\tilde{\Gamma}/\Gamma_\infty$, the dimensionless tangent shear stress on the bubble surface, $\tau_{nt}d/(V_b\mu_c)$, the dimensionless surfactant concentration inside the liquid adjacent to the bubble surface, C/C_∞, and the dimensionless gas–liquid relative velocity on the bubble surface, V_s/V_b, where $V_s = (V_b - \boldsymbol{v}\cdot\boldsymbol{t})$ are plotted as functions of the axial coordinate, z, for different values of La and with $Re = 0.25$, $Ca = 0.01$, and $d/d_h = 0.75$. Note that the origin of the axial coordinate, $z = 0$, is at the back of the bubble. As described previously, the recirculating flow in between bubbles causes surfactants to accumulate near the convergent stagnation point/circle on the bubble surface and to deplete near the divergent stagnation point/circle. This is confirmed by Figure 6a. Notably, for $La = 0.1$, the adsorption flux of surfactants toward the bubble surface is not sufficient to maintain surfactants around the divergent stagnation circle on the front half of the bubble side (point D in Figure 5) and, consequently, the bubble surface is almost clean of surfactants near this divergent stagnation circle. The tangent shear stress distribution on the bubble surface is shown in Figure 6b. It can be observed that the shear stress increases as La is increased. The shear stress is positive on the side of the bubble and becomes negative at the back and at the front of the bubble. At the front of the bubble, near the convergent stagnation point on the bubble surface (point A in Figure 5), surfactants accumulate. On the contrary, near the divergent stagnation circle on the front half of the bubble (point D in Figure 5), surfactants are depleted. This creates a Marangoni stress directed toward the back of the bubble, as sketched in Figure 5, leading to the negative values of τ_{nt} at the front of the bubble for $La > 0$ (see Figure 6b). A Marangoni stress directed toward the back of the bubble is also generated between C and B, for $La > 0$ (see Figure 6b). On the other hand, as shown in Figure 6b, on the side of the bubble, for $La > 0$, a Marangoni stress induced in between the divergent stagnation circle and the convergent one is directed toward the front of the bubble, as sketched in Figure 5. It is observed in Figure 6b that the tangent shear stress reaches a maximum on the side of the bubble, where the gap between the bubble and the channel wall is the smallest. For $La = 0.1$, as discussed previously, the surfactant adsorption toward the interface is small when compared with the advective flux of the surfactant from the divergent stagnation circle to the convergent stagnation one. As a consequence, the shear stress on the bubble surface does not increase significantly on the front part of the bubble when La is increased from 0 to 0.1. It is observed in Figure 6b that the tangent shear stress, τ_{nt}, becomes independent of La when $La > 1$. It should be noted that $\tau_{nt}d/(V_b\mu_c)$ reaches its maximum value at locations on the bubble surface where $\nabla\tilde{\Gamma}$ is the highest. For instance, the shear stress profile on the bubble surface presented in Figure 6b, for $La = 0.1$, exhibits a maximum at $z \approx 0.75$ mm. At that location on the bubble surface, $\tilde{\Gamma}/\Gamma_\infty$ exhibits an important gradient, as it can be observed in Figure 6a, for $La = 0.1$. This can be

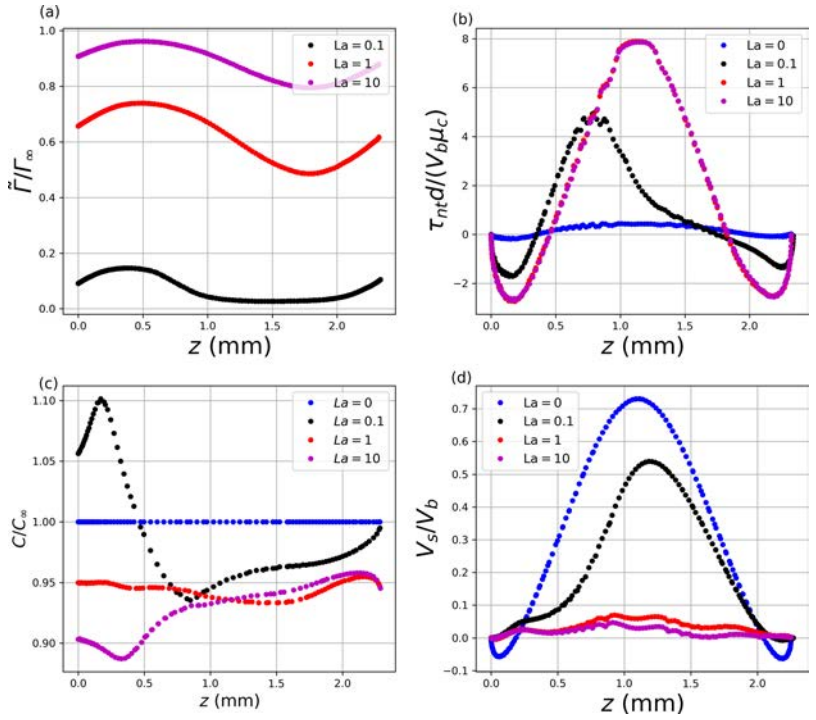

Figure 6. (a) Dimensionless surfactant concentration on the bubble surface, Γ/Γ_∞, (b) dimensionless shear stress tangent to the bubble surface, $\tau_{nt}d/(V_b\mu_c)$, (c) dimensionless surfactant concentration inside the liquid adjacent to the bubble surface, C/C_∞, and (d) dimensionless liquid velocity tangent to the bubble surface, V_s/V_b, as functions of the axial coordinate, z, for different value of La; $z = 0$ is at the back of the bubble. The other dimensionless numbers are fixed to $Re = 0.25$, $Ca = 0.01$, and $d/d_h = 0.75$.

rationalized by writing the tangent shear stress balance at the interface, neglecting the viscosity of the gas phase: $\tau_{nt} = \nabla_s\sigma\cdot\boldsymbol{t}$, where $\nabla_s\sigma$ can be linked to the gradient of $\tilde{\Gamma}$ through eq 24. It might be expected that the Marangoni stresses induced by the interaction between the flow structure and surfactants tend to immobilize (in a reference frame attached to the bubble) the bubble surface for large values of La. This is characterized in Figure 6d, where V_s/V_b is plotted against the axial coordinate, z. When $La = 0$, the surface velocity is positive on the side of the bubble and changes sign near the front and the back of the bubble because of the recirculating flow. When La is increased to 0.1, the fluid velocity is significantly reduced on the side of the bubble. Moreover, V_s is also significantly modified on the front/back of the bubble. For instance, V_s/V_b reaches almost the value of 0 in between the convergent stagnation point and the divergent stagnation circle on the front half of the bubble side (between A and D in Figure 5): the Marangoni stress induced in between the convergent stagnation point and the divergent stagnation circle tends to immobilize the interface, in this region, when La is increased from 0 to 0.1. As La is increased to 1, V_s approaches 0 everywhere on the bubble surface: the Marangoni stress created in between the convergent stagnation circle (C in Figure 5) and the divergent one (D in Figure 5) leads almost to the interface immobilization.

The surfactants induce an immobilization of the bubble surface (in a reference frame attached to the bubble) through the mechanisms discussed in the previous paragraph. Thus, it might be expected that the surfactants have a significant impact on the velocity of the spherical bubble. An important parameter in microfluidic bubbly flow is the ratio of the bubble velocity, V_b, to the mean flow velocity, J_l. Mikaelian et al. (2015) established correlations, valid for an isolated spherical bubble (i.e., for $Ca \to 0$), to calculate this ratio as a function of d/d_h, for two limiting situations:[20] (i) They imposed a stress free condition on the bubble surface to model a situation without surfactants. They proposed eq 1 to calculate V_b/J_l in this limiting situation. (ii) They imposed a no slip condition at the bubble surface to model the influence of surfactants. They proposed eq 2 to calculate V_b/J_l in this situation. The ratio V_b/J_l is presented in Figure 7 as a function of d/d_h, for different values of La and for $Ca = 0.01$ and $Re = 0.25$. Equations 1 and 2 are represented in this figure as the blue and red solid lines, respectively. Squares give values calculated with JADIM for $La = 0$, 0.1, 1, and 10. It is observed that the two limiting cases are well reproduced by our

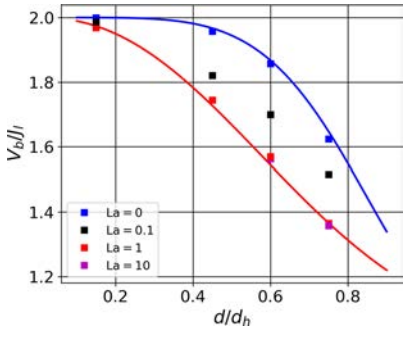

Figure 7. Ratio of the bubble velocity to the mean flow velocity, V_b/J_l, as a function of the ratio of the bubble diameter to the channel diameter, d/d_h. Blue and red solid lines are the correlations established numerically by Mikaelian et al. (2015) for a stress free and an immobile interface, respectively. Squares give values obtained with JADIM, for different values of La and for $Re = 0.25$ and $Ca = 0.01$.

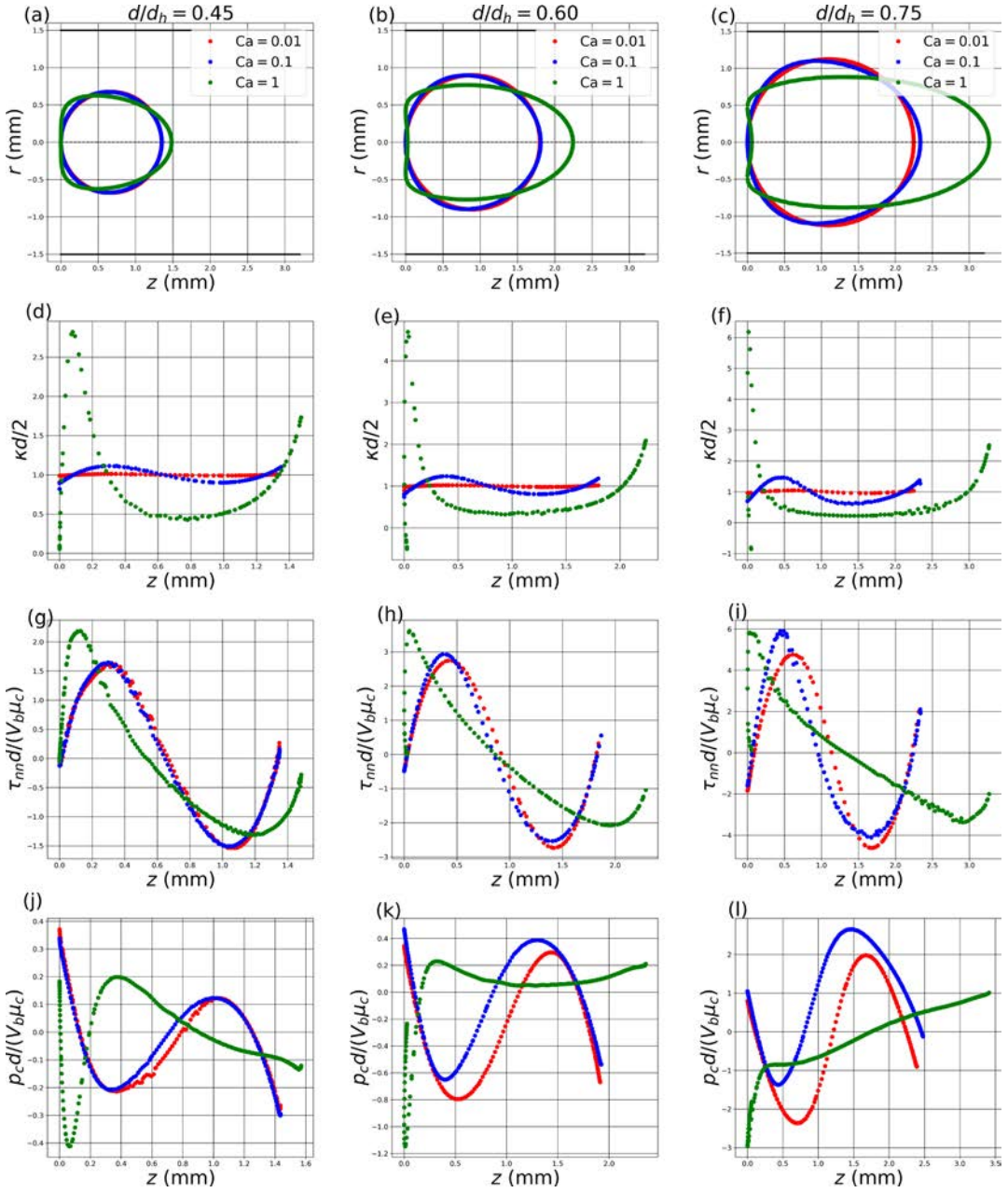

Figure 8. (first row) Radial position of the interface as a function of z. (second row) Normalized curvature, $\kappa d/2$, as a function of z. (third row) Dimensionless normal viscous stress on the bubble surface, $\tau_{nn}d/(V_b\mu_c)$, as a function of z. (fourth row) Dimensionless liquid pressure on the bubble surface, $p_c d/(V_b\mu_c)$, as a function of z. The different columns correspond to (first column) $d/d_h = 0.45$, (second column) $d/d_h = 0.6$ and (third column) $d/d_h = 0.75$, respectively. Red dots: $Ca = 0.01$, blue dots: $Ca = 0.1$, green dots: $Ca = 1$. These results have been obtained for a clean interface, that is, $La = 0$.

simulations, for $La = 0$ and $La = 1$. An intermediate value of V_b/J_l is obtained for $La = 0.1$. In line with the observations in the previous paragraph, V_b/J_l becomes independent of La for $La > 1$: the value of V_b/J_l that characterizes a bubble behaving as a rigid sphere is obtained for $La > 1$. It is worth pointing out that, as seen in the previous section, a spherical bubble rising in a stagnant liquid of infinite extent containing surfactants behaves also as a rigid sphere regarding its velocity when $La \geq 1$. The analysis of the velocity field for the different cases shows that recirculations at the front and at the back of the bubble are present for all of the cases presented in Figure 7, except for the one with $La = 0$ and $d/d_h = 0.15$. This is coherent with the results of Mikaelian et al. (2015).

Deformable Bubble without Surfactant. In this subsection, the bubble shape, the bubble drag coefficient, C_d, and the ratio of the bubble velocity to the mean flow velocity, V_b/J_l, are analyzed without surfactants. Accordingly, Ca is varied between 0.01 and 1, with $La = 0$. The bubble shape is characterized by plotting the (r,z) coordinates of the bubble interface as well as by computing the curvature of its interface: $\kappa = -\nabla\cdot(\nabla\phi/\nabla\phi)$. Results regarding the bubble shape are presented in Figure 8a–c, for $d/d_h = 0.45$, 0.6, and 0.75, respectively. The red ($Ca = 0.01$ and $Re = 0.25$), blue ($Ca = 0.1$ and $Re = 1$), and green ($Ca = 1$ and $Re = 1$) symbols give values of the (r,z) coordinates of the bubble interface. It is observed that the shape of the bubble is nearly spherical for Ca

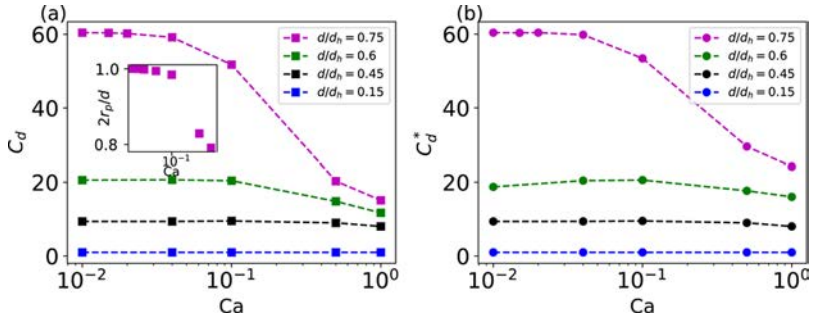

Figure 9. (a) Drag coefficient, $C_d = 4F_d/(0.5(V_b - J_l)^2\pi d^2)$, as a function of Ca, for $La = 0$ and for different values of d/d_h. (b) Drag coefficient based on the effective projection area of the bubble on a plane perpendicular to the main flow direction, $C_d^* = F_d/(0.5(V_b - J_l)^2\pi r_p^2)$, as a function of Ca, for $La = 0$ and for different values of d/d_h.

= 0.01 and Ca = 0.1, for all values of d/d_h. However, when Ca = 1, the bubble is elongated and takes a "bullet shape". This shape is further characterized in Figure 8d–f, where the curvature, κ, of the gas–liquid interface is plotted as a function of the axial coordinate, z. The curvature κ is normalized by the curvature of a spherical bubble that has the same volume: $2/d$. When Ca = 0.01, the curvature of the bubble is constant and equal to $2/d$, regardless of the value of d/d_h, as depicted by the red dots in Figure 8d–f. When Ca = 0.1, κ is not constant along the bubble interface. For example, the dimensionless curvature profile shown in Figure 8f for Ca = 0.1 (Re = 1, d/d_h = 0.75) exhibits a value larger than one at $z \approx 0.5$ mm ($\kappa d/2 \approx 1.5$) and a value smaller than one at $z \approx 1.5$ mm ($\kappa d/2 \approx 0.75$). At the front of the bubble, $\kappa d/2$ is also larger than one and at the back, it is smaller than one. For Ca = 1 (Re = 1, d/d_h = 0.75, Figure 8f), the normalized curvature is reduced all along the body of the bubble except near its front and its back.

The dimensionless normal viscous stress on the interface, $\tau_{nn}d/(V_b\mu_c)$, is plotted against the axial coordinate, z, in Figure 8g–i, for d/d_h = 0.45, 0.6, and 0.75, respectively. Note that a negative value of $\tau_{nn}d/(V_b\mu_c)$ indicates a stress directed from the liquid toward the bubble interface (i.e., "pushing" the interface). On the contrary, a positive value of $\tau_{nn}d/(V_b\mu_c)$ indicates a normal stress directed from the interface toward the liquid phase (i.e., "pulling" the interface). It is observed that $\tau_{nn}d/(V_b\mu_c)$ is below zero near the divergent stagnation circle on the bubble surface on the front half of the bubble. On the contrary, $\tau_{nn}d/(V_b\mu_c)$ is higher than zero near the convergent stagnation circle on the bubble surface, on the back half of the bubble. Finally, in Figure 8j–l), the periodic component of the dimensionless pressure in the liquid on the interface, $p_c d/(V_b\mu_c)$, is plotted as a function of z. It is observed that $-p_c$ and τ_{nn} roughly follow the same trends, $-p_c$ being significantly smaller than τ_{nn} for the cases reported here. The normal stress balance at the bubble–liquid interface is written, for moderate values of Re, neglecting the viscosity of the gas phase, in dimensionless form, as

$$\bar{p}_d - \bar{p}_c + \bar{\tau}_{nn} \approx \frac{1}{Ca_b}\bar{\kappa} \tag{31}$$

where $p_d = p_d d/(V_b\mu_c)$ is the periodic component of the dimensionless pressure in the gas on the interface, $p_c = p_c d/(V_b\mu_c)$, $\tau_{nn} = \tau_{nn}d/(V_b\mu_c)$, $\kappa = \kappa d$, and $Ca_b = \mu_c V_b/\sigma_0$. Equation 31 shows that as p_d is almost constant, an increase of p_c or a decrease of τ_{nn} leads to a decrease of κ. Reciprocally, a decrease of p_c or an increase of τ_{nn} leads to an increase of κ. This can be observed by comparing Figure 8d,g, e,h, and f,i. The recirculating flow in between bubbles generates points (or circles) on the bubble surface where the normal viscous stress is locally negative, near the divergent stagnation point (or circle), or positive, near the convergent stagnation point (or circle). Thus, eq 31 shows that as Ca_b (or similarly Ca) is increased, the inhomogeneous distribution of the normal viscous stress (and pressure) on the bubble surface, generated by the recirculating flow, causes the curvature of the bubble surface to decrease near the divergent stagnation point (or circle) and to increase near the convergent stagnation point (or circle). This leads to the elongation of the bubble as Ca is increased.

Because of the recirculating flow in between bubbles, the bubble elongates as Ca is increased in contrast to the case of a bubble rising in a stagnant liquid of infinite extent where the bubble is flattened. Thus, the drag coefficient of the bubble based on its equivalent diameter and on the bubble liquid relative velocity, $C_d = 4F_d/(1/2(V_b - J_l)^2\pi d^2)$ is expected to be affected by the deformability of the bubble in a particular way. The drag force acting on the bubble, F_d, is computed as presented in the validation section. C_d is plotted in Figure 9a as a function of Ca, for d/d_h = 0.15, 0.45, 0.6, and 0.75, respectively. Note that the values of the drag coefficient computed with JADIM are in good agreement with the ones deduced from calculations obtained by Rivero Rodriguez and Scheid (2018). It is observed that, in general, the drag coefficient of the bubble decreases as d/d_h decreases. It is observed that C_d is almost constant with respect to Ca when $d/d_h < 0.45$. However, for larger values of this ratio, C_d decreases when Ca gets larger than 0.1. To understand this effect, the radius of the projection of the bubble on a plane perpendicular to the z axis, r_p, is plotted against Ca in a small inset in Figure 9a. As the capillary number is increased from 0.1 to 1, r_p decreases from $d/2$ to less than $0.8d/2$. As discussed in the previous paragraph, the recirculating flow in between bubbles causes the bubble to elongate for $Ca \approx 1$. As the bubble elongates, r_p decreases leading to the reduction of the drag force acting on the bubble. This partly explains why C_d decreases when Ca is increased, as C_d is defined using the equivalent diameter, d. An alternative drag coefficient can be defined using πr_p^2 as the reference surface: $C_d^* = F_d/(0.5(V_b - J_l)^2\pi r_p^2)$. This alternative drag coefficient is plotted as a function of Ca in Figure 9b. It is observed that C_d and C_d^* exhibits the same kind of evolution with respect to Ca, though C_d^* is slightly less affected by Ca than C_d. This indicates that the change in the distribution of the pressure and of the normal viscous stress on the bubble surface induced when increasing Ca (see Figure 8g–l)) is mainly responsible for the

reduction of C_d. Notably, it is shown in the next section that the convergent stagnation circle on the front half of the bubble disappears when Ca is increased beyond $Ca \approx 0.5$.

C_d is reduced as Ca is increased, especially for values of $d/d_h > 0.6$. Thus, the effect of Ca on V_b/J_l is expected to be significant, especially for values of $d/d_h > 0.6$. In Figure 10, V_b/J_l is plotted as a function of d/d_h, for $Ca = 0.01$, $Ca = 0.1$, $Ca = 0.5$, and $Ca = 1$. V_b/J_l decreases as d/d_h increases when $Ca = 0.01$ and $Ca = 0.1$. However, when $Ca = 0.5$ or $Ca = 1$, it is observed that V_b/J_l increases and takes a value larger than 2 as d/d_h is increased. Furthermore, at a constant value of d/d_h, increasing Ca leads to an increase of V_b/J_l. For instance, when $d/d_h = 0.75$, V_b/J_l increases from 1.6 to 2.2 when Ca is increased from 10^{-2} to 1.

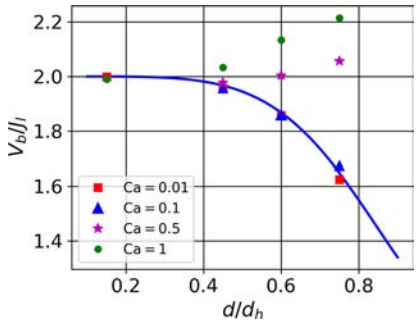

Figure 10. V_b/J_l as a function of d/d_h, for $Ca = 0.01$, $Ca = 0.1$, $Ca = 0.5$, and $Ca = 1$ depicted by squares, triangles, stars, and circles, respectively. There is no surfactant in the system. The blue solid line is the correlation established numerically by Mikaelian et al. (2015), predicting the value of V_b/J_l for a bubble having a clean surface.

Deformable Bubble with Surfactants. In this sub section, the combined effect of La and Ca on the bubble dynamics is analyzed for $d/d_h = 0.75$. The steady state surfactant concentration on the surface, $\tilde{\Gamma}$, (presented at the vicinity of the bubble surface only) and in the liquid, C, are presented in Figure 11, for $d/d_h = 0.75$, $Re = 1$, $Ca = 0.5$, (a) $La = 0$, (b) $La = 0.1$, (c) $La = 1$, and (d) $La = 10$. It is observed that the bubble is elongated and that recirculations have disappeared when compared with the cases presented in Figure 4. As a consequence, only two stagnation points remain on the bubble surface, one at the front of the bubble and one at the back. Surfactants are swept to the back of the bubble and accumulate there, leading to a clean interface on the front half of the bubble. Consequently, surfactants desorb from the surface at the back of the bubble leading to their accumulation in the liquid adjacent to the back of the bubble. As La is increased from 0.1 to 1, more surfactants are adsorbed on the bubble surface and, consequently, more surfactants accumulate at the back of the bubble. This leads to a slight invagination of the back of the bubble. When $La = 10$, it appears that the invagination proceeds toward the front of the bubble and finally leads to the bursting of the bubble. Because of the change in the flow structure, the divergent stagnation circle on the bubble surface, where the liquid pressure, p_c, and the normal viscous stresses, τ_{nn}, were contributing to increase the drag coefficient of the bubble (see Figure 8), disappears. This might explain the diminution of the drag coefficient C_d* when Ca is increased (see Figure 9) and the consequent increase in V_b/J_l.

The results presented in Figure 11 show that the deformation of the bubble, when $Ca = 0.5$, has a strong influence on the structure of the flow near the bubble, when compared with a spherical bubble. This, in turn, has a significant influence on the distribution of the surfactants on the surface of the bubble. To give more insights into this, $\tilde{\Gamma}/\Gamma_\infty$ is plotted as a function of the axial coordinate, z, with $z = 0$ at the back of the bubble, in the first column of Figure 12, for $Ca = 0.04$ (first row), $Ca = 0.1$ (second row), and $Ca = 0.5$ (third row), for $d/d_h = 0.75$ and for different values of La. For $Ca = 0.04$, the bubble is almost spherical, and as mentioned previously, it is observed that the surfactants accumulate near the convergent stagnation point/circle on the bubble surface and are depleted near the divergent stagnation point/circle. When Ca is equal to 0.1, a similar distribution of the surfactants on the surface of the bubble is observed, but with steeper gradients. Finally, when Ca is equal to 0.5, it is observed that the surfactants are totally swept to the back of the bubble.

Increasing Ca induces a change in the flow field around the bubble and a consequent change in the surfactant distribution on the bubble surface. Thus, it might be expected that the tangent shear stress distribution on the bubble surface, $\tau_{nt}d/(V_b\mu_c)$, is also strongly affected by an increase of Ca. On the second column of Figure 12, $\tau_{nt}d/(V_b\mu_c)$ is presented as a function of the axial coordinate, z, for different values of Ca and La. As Ca increases from 0.04 to 0.1, the surfactant concentration decreases near the divergent stagnation circle on the front part of the bubble side, causing a decrease of the shear stress at that location, for $La = 1$ and $La = 10$. As Ca is increased further, all of the surfactants accumulate at the back

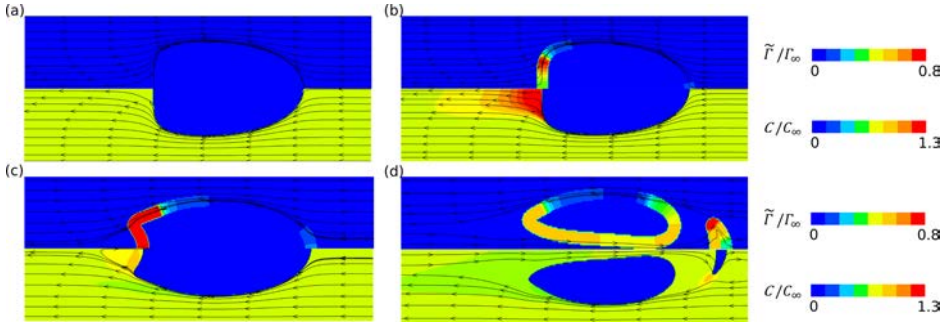

Figure 11. Contour plots of the surfactant concentration field, $\tilde{\Gamma}$, (upper part) and the bulk surfactant concentration field, C (lower part), for $Ca = 0.5$, $d/d_h = 0.75$ and (a) $La = 0$, (b) $La = 0.1$, (c) $La = 1$, and (d) $La = 10$. Velocity streamlines are drawn in a reference frame translating with the bubble velocity. The bubbles move from left to right. Note that the bubble sketched in (d) has burst and might not have reached its terminal shape.

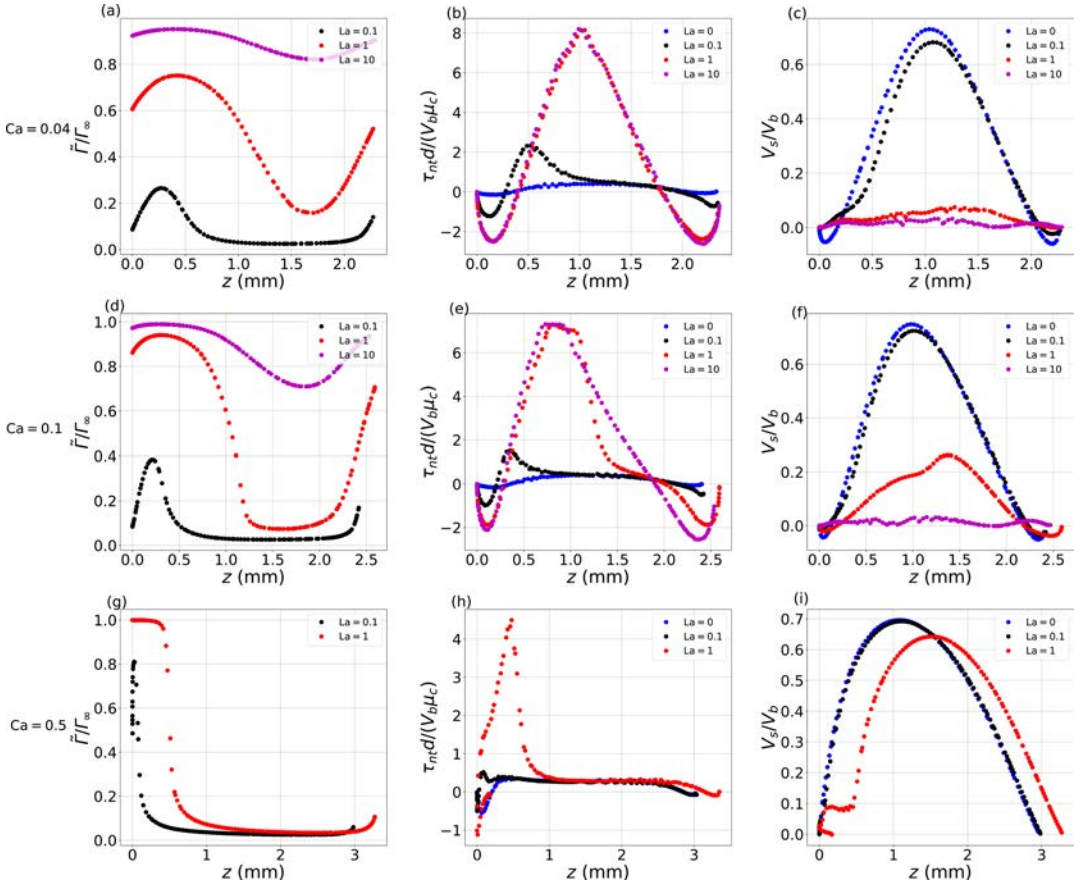

Figure 12. (first column) Surfactant concentration on the surface of the bubble, $\tilde{\Gamma}/\Gamma_\infty$, (second column) viscous shear stress along the tangent to the bubble surface, $\tau_{nt}d/(V_b\mu_c)$, and (third column) ratio of the liquid velocity tangent to the bubble surface to the bubble velocity, V_s/V_b. (first line) Ca = 0.04, (second line) Ca = 0.1 and (third line) Ca = 0.5.

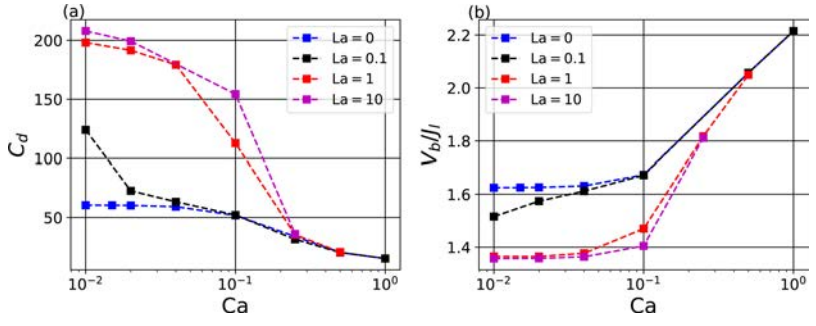

Figure 13. (a) Drag coefficient as a function of Ca for d/d_h = 0.75 and different values of La. (b) V_b/J_l as a function of Ca for d/d_h = 0.75 and different values of La.

of the bubble leading to a clean surface on the most part of the bubble, except at the back.

The tangent shear stress distribution on the bubble surface is expected to affect the interface velocity. On the third column of Figure 12, V_s/V_b is presented as a function of z, for different values of Ca and La. It is observed that, in general, increasing La leads to the reduction of V_s/V_b. It is reduced at locations where the shear stress on the bubble surface is high. For example, the shear stress profile observed for Ca = 0.04 and La = 0.1 (black dots in Figure 12b) exhibits a peak at $z \approx 0.5$ mm, where the concentration profile of surfactants exhibits an important gradient (black dots in Figure 12a). The influence of La on V_s/V_b is reduced for Ca = 0.5 (see Figure 12i). As mentioned previously, as Ca is increased, surfactants are swept to the back of the bubble and consequently have a smaller influence on V_s/V_b.

The drag coefficient of the bubble, $C_d = 4F_d/(0.5\rho_c(V_b - J_l)^2\pi d^2)$, is also expected to be less influenced by the presence of surfactants when Ca is increased. The effect of Ca and La on the drag coefficient of the bubble is analyzed in Figure 13a, where C_d is plotted as a function of Ca for several values of La and for d/d_h = 0.75. It is observed that, in general, the drag coefficient of the bubble increases with La. As it might have been expected, when Ca is larger than approximately 0.5, the drag coefficient of the bubble becomes almost independent of La. As for C_d, V_b/J_l becomes also independent of La when Ca is larger than 0.5, as it can be observed in Figure 13b.

The bubble velocity and the drag coefficient becomes independent of La as Ca reaches values close to unity, for $d/d_h = 0.75$. At this point, surfactants accumulate at the back of the bubble and reduce locally the surface tension of the gas–liquid interface. This causes the back of the bubble to deform, as illustrated in Figure 11b. Increasing La further causes the back of the bubble to invaginate. This can even cause the bubble to burst, as presented in Figure 14. This unsteady bursting

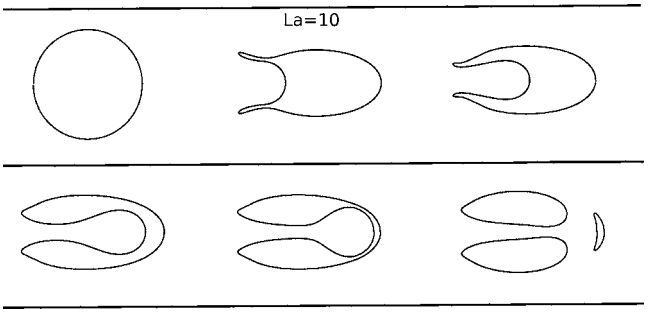

Figure 14. Contours of the bubble at different time for $La = 10$, $d/d_h = 0.75$, and $Ca = 0.5$.

phenomenon reported in Figure 14 was also observed in previous experimental and numerical studies that considered the effect of viscosity ratio (λ) on the shape and bursting behavior of drops.[43,44]

In the previous section, eq 31 was used to discuss the change in bubble shape with Ca. The same equation can be used to discuss the effect of La on the bubble shape. As seen in the previous paragraph, as Ca reaches values close to 0.5, surfactants are swept to the back of the bubble and consequently reduce locally the surface tension of the gas–liquid interface. If eq 31 is evaluated at the back of a bubble (a bubble such as the one in Figure 11a,b or c), with $\kappa \approx 2/r_c$, where r_c is the radius of curvature of the back of the bubble, an expression of r_c can obtained

$$r_c = \frac{2d}{(\overline{p}_d - \overline{p}_c + \overline{\tau}_{nn})Ca_b\frac{\sigma_0}{\sigma}} \tag{32}$$

In contrast to eq 31, the presence of the surfactant is considered, and consequently, the effective surface tension of the gas–liquid interface appears in eq 32. The periodic component of the pressure inside the gas can be estimated as $p_d = 4\sigma/d$. In the dimensionless form, it gives $p_d = 4/(Ca_b\sigma_0/\sigma)$. Thus, eq 32 yields

$$r_c = \frac{2d}{4 + (-\overline{p}_c + \overline{\tau}_{nn})Ca_b\frac{\sigma_0}{\sigma}} \tag{33}$$

It should be noted that when $Ca_b \to 0$, the bubble is spherical and $r_c = d/2$ is recovered from eq 33. At the back of the bubble, $-p_c + \tau_{nn}$ is negative (see Figure 8). Thus, as Ca_b increases, the normal stresses at the back of the bubble cause r_c to increase, and consequently the back of the bubble flattens. As it is increased further, r_c might change sign if $|(-p_c + \tau_{nn})Ca_b\sigma_0/\sigma| > 4$. This causes the back of the bubble to invaginate. As it can be seen in eq 33, the same effect can be caused by surfactants accumulating at the back of the bubble because the presence of surfactants increases σ_0/σ. Equation 33 also shows that the increase of Ca_b and/or σ_0/σ can lead to the bubble bursting if r_c approaches negative values close to zero. In Figure 15, r_c is plotted as a function of Ca, for $\sigma/\sigma_0 = 0$ and 0.5.

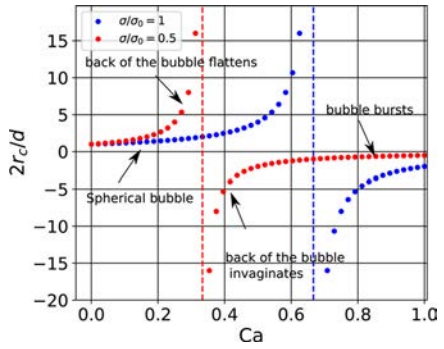

Figure 15. r_c as a function of Ca for different values of σ/σ_0. The dashed vertical lines depict vertical asymptotes.

In this figure, $-p_c + \tau_{nn}$ is imposed to -3. $-p_c + \tau_{nn} = -3$ characterizes the normal viscous stresses at the back of a bubble with $d/d_h = 0.75$ and $Ca = 0.01$ and 0.1 (see Figure 8i,l). The blue and red vertical lines depict the critical value of Ca from which the back of the bubble begins to invaginate. In Figure 15, it is visible that increasing Ca causes the back of the bubble to flatten and to invaginate. If there are surfactants in the system, $0 < \sigma_0/\sigma < 1$. The case of $\sigma/\sigma_0 = 0.5$ is presented in Figure 15. In this case, for $Ca \to 1$, r_c approaches 0 (being negative) indicating a bubble with a severe invagination on its back. In this case, the bubble probably bursts.

As an example, a diagram presenting the different regimes obtained in the simulations for $d/d_h = 0.75$ is presented in Figure 16. In this plot, three distinct regions can be identified,

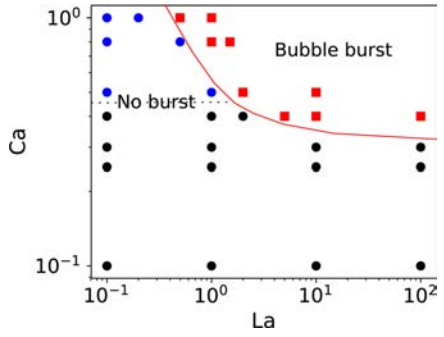

Figure 16. Bubble stability diagram for $d/d_h = 0.75$. Black, blue, and red symbols represent a simulation where $V_b/J_l < 2$, $V_b/J_l > 2$, and the bubble bursts, respectively.

corresponding to classical bubble motion with $V_b/J_l < 2$, bubble with velocity larger than the maximum velocity in the liquid, that is, $V_b/J_l > 2$, and unstable bubble, leading to burst. This figure illustrates a transition between a bursting bubble and a stable bubble (red solid line in Figure 16). As it can be observed, this transition depends upon the bubble deform ability (i.e., upon Ca), and surfactants (i.e., upon La). This transition might also depend on other nondimensional numbers characterizing the surfactants. However a complete parametric study is beyond the scope of this paper.

CONCLUSION

We performed a numerical study to investigate the effect of soluble surfactants and deformability on the dynamics of a small bubble translating in a horizontal microchannel of circular cross section. We use an LS method to capture the gas–liquid interface. The capillary pressure jump and the

Marangoni stress are computed using the CSF model. The transport of surfactants on the bubble surface is dealt in an Eulerian framework and is coupled to its transport in the liquid.

In line with previous studies, we observed that when the bubble is spherical, the liquid recirculates in between bubbles. As a consequence, surfactants accumulate on convergent stagnation point/circle on the bubble surface and deplete on divergent stagnation point/circle. For a Langmuir number larger than 1, this causes the bubble interface to get almost immobilized in between convergent and divergent stagnation points/circles (in a reference frame attached to the bubble) because of Marangoni stresses induced by surface tension gradients; regarding its velocity relative to the liquid, the bubble behaves as a solid sphere when $La > 1$. The ratio of the bubble velocity to the mean flow velocity decreases as the ratio of the bubble diameter to the tube diameter increases. Furthermore, when the bubble is spherical, it is shown that surfactants can increase the drag coefficient of the bubble by a factor of 2.

When the bubble is allowed to deform, that is, when the capillary number is of order of unity, the curvature of its interface is reduced near the divergent stagnation circle on the front part of the bubble side, where the viscous stress normal to the bubble surface is high. This is due to the recirculating flow, which "hits" the bubble at this location, and locally increases this stress. Consequently, it reduces the curvature of the bubble interface. Therefore, the bubble elongates as Ca is increased. As the bubble elongates, it is shown that its drag coefficient decreases due to the modification of the flow structure around the bubble. Consequently, the ratio of its velocity to the mean liquid velocity, V_b/J_l, increases and can be larger than 2. For $d/d_h = 0.75$, if Ca becomes larger than approximately 0.5, recirculations in between bubbles disappear and surfactants are swept toward the back of the bubble. They have less influence on the drag coefficient of the bubble and on its velocity than for a spherical bubble. Increasing the amount of surfactant adsorbing to the bubble surface can eventually cause the back of the bubble to invaginate and possibly the bubble to burst.

AUTHOR INFORMATION

Corresponding Authors

*E mail: oatasi@ulb.ac.be (O.A.).

*E mail: dominique.legendre@imft.fr (D.L.).

ORCID

O. Atasi: 0000 0003 4957 3996

ACKNOWLEDGMENTS

Some of the computational time was provided by the Scientific Groupment CALMIP (project no. P17006), the contribution of which is greatly appreciated. We are grateful to Javier Rivero rodriguez for useful discussions. O.A. and B.S. thank the F.R.S FNRS for the financial support. O.A. thanks the "Jaumotte−Demoulin" and "David et Alice Van Buuren" funds for partly founding this project.

REFERENCES

(1) Han, Y.; Liu, Y.; Li, M.; Huang, J. A review of development of micro channel heat exchanger applied in air conditioning system. *Energy Procedia* 2012, *14*, 148−153.

(2) Kashid, M. N.; Renken, A.; Kiwi Minsker, L. Gas liquid and liquid liquid mass transfer in microstructured reactors. *Chem. Eng. Sci.* 2011, *66*, 3876−3897.

(3) Hassanvand, A.; Hashemabadi, S. H. Direct numerical simulation of mass transfer from Taylor bubble flow through a circular capillary. *Int. J. Heat Mass Transfer* 2012, *55*, 5959−5971.

(4) Abiev, R. S. Bubbles velocity, Taylor circulation rate and mass transfer model for slug flow in milli and microchannels. *Chem. Eng. J.* 2013, *227*, 66−79.

(5) Abadie, T.; Aubin, J.; Legendre, D.; Xuereb, C. Hydrodynamics of gas liquid Taylor flow in rectangular microchannels. *Microfluid. Nanofluid.* 2012, *12*, 355−369.

(6) Gupta, R.; Fletcher, D. F.; Haynes, B. S. CFD modelling of flow and heat transfer in the Taylor flow regime. *Chem. Eng. Sci.* 2010, *65*, 2094−2107.

(7) Yu, Z.; Hemminger, O.; Fan, L. S. Experiment and lattice Boltzmann simulation of two phase gas liquid flows in microchannels. *Chem. Eng. Sci.* 2007, *62*, 7172−7183.

(8) Cubaud, T.; Sauzade, M.; Sun, R. CO2 dissolution in water using long serpentine microchannels. *Biomicrofluidics* 2012, *6*, 022002.

(9) Feng, J. Q. Steady axisymmetric motion of a small bubble in a tube with flowing liquid. *Proc.: Math., Phys. Eng. Sci.* 2010, *466*, 549−562.

(10) Khodaparast, S.; Magnini, M.; Borhani, N.; Thome, J. R. Dynamics of isolated confined air bubbles in liquid flows through circular microchannels: an experimental and numerical study. *Microfluid. Nanofluid.* 2015, *19*, 209−234.

(11) Kurimoto, R.; Hayashi, K.; Tomiyama, A. Terminal velocities of clean and fully contaminated drops in vertical pipes. *Int. J. Multiphase Flow* 2013, *49*, 8−23.

(12) Stan, C. A.; Guglielmini, L.; Ellerbee, A. K.; Caviezel, D.; Stone, H. A.; Whitesides, G. M. Sheathless hydrodynamic positioning of buoyant drops and bubbles inside microchannels. *Phys. Rev. E: Stat., Nonlinear, Soft Matter Phys.* 2011, *84*, 036302.

(13) Fdhila, R. B.; Duineveld, P. C. The effect of surfactant on the rise of a spherical bubble at high Reynolds and Peclet numbers. *Phys. Fluids* 1996, *8*, 310−321.

(14) Cuenot, B.; Magnaudet, J.; Spennato, B. The effects of slightly soluble surfactants on the flow around a spherical bubble. *J. Fluid Mech.* 1997, *339*, 25−53.

(15) Tasoglu, S.; Demirci, U.; Muradoglu, M. The effect of soluble surfactant on the transient motion of a buoyancy driven bubble. *Phys. Fluids* 2008, *20*, 040805.

(16) Takagi, S.; Ogasawara, T.; Fukuta, M.; Matsumoto, Y. Surfactant effect on the bubble motions and bubbly flow structures in a vertical channel. *Fluid Dyn. Res.* 2009, *41*, 065003.

(17) Fukuta, M.; Takagi, S.; Matsumoto, Y. Numerical study on the shear induced lift force acting on a spherical bubble in aqueous surfactant solutions. *Phys. Fluids* 2008, *20*, 040704.

(18) Baret, J. C.; Kleinschmidt, F.; El Harrak, A.; Griffiths, A. D. Kinetic Aspects of Emulsion Stabilization by Surfactants: A Microfluidic Analysis. *Langmuir* 2009, *25*, 6088−6093.

(19) Riaud, A.; Zhang, H.; Wang, X.; Wang, K.; Luo, G. Numerical Study of Surfactant Dynamics during Emulsification in a T Junction Microchannel. *Langmuir* 2018, *34*, 4980−4990.

(20) Mikaelian, D.; Haut, B.; Scheid, B. Bubbly flow and gas liquid mass transfer in square and circular microchannels for stress free and rigid interfaces: CFD analysis. *Microfluid. Nanofluid.* **2015**, *19*, 523−545.
(21) Rivero Rodriguez, J.; Scheid, B. Bubble dynamics in micro channels: inertial and capillary migration forces. *J. Fluid Mech.* **2018**, *842*, 215−247.
(22) Dupont, J. B.; Legendre, D. Numerical simulation of static and sliding drop with contact angle hysteresis. *J. Comput. Phys.* **2010**, *229*, 2453−2478.
(23) Abadie, T.; Aubin, J.; Legendre, D. On the combined effects of surface tension force calculation and interface advection on spurious currents within Volume of Fluid and Level Set frameworks. *J. Comput. Phys.* **2015**, *297*, 611−636.
(24) Legendre, D.; Magnaudet, J. The lift force on a spherical bubble in a viscous linear shear flow. *J. Fluid Mech.* **1998**, *368*, 81−126.
(25) Legendre, D.; Magnaudet, J.; Mougin, G. Hydrodynamic interactions between two spherical bubbles rising side by side in a viscous liquid. *J. Fluid Mech.* **2003**, *497*, 133−166.
(26) Scardovelli, R.; Zaleski, S. Direct Numerical Simulation of Free Surface and Interfacial Flow. *Annu. Rev. Fluid Mech.* **1999**, *31*, 567−603.
(27) Stone, H. A. A simple derivation of the time dependent convective diffusion equation for surfactant transport along a deforming interface. *Phys. Fluids A* **1990**, *2*, 111−112.
(28) Batchelor, G. K. *An Introduction to Fluid Dynamics*; Cambridge University Press, 1967.
(29) Muradoglu, M.; Tryggvason, G. A front tracking method for computation of interfacial flows with soluble surfactants. *J. Comput. Phys.* **2008**, *227*, 2238−2262.
(30) Levich, V. *Physicochemical Hydrodynamics*; Prentice Hall, 1962.
(31) Takemura, F. Adsorption of surfactants onto the surface of a spherical rising bubble and its effect on the terminal velocity of the bubble. *Phys. Fluids* **2005**, *17*, 048104.
(32) Abadie, T. Hydrodynamics of Gas−Liquid Taylor Flow in Microchannels. Ph.D. Thesis, University of Toulouse, 2013.
(33) Osher, S.; Sethian, J. A. Fronts propagating with curvature dependent speed: Algorithms based on Hamilton Jacobi formulations. *J. Comput. Phys.* **1988**, *79*, 12−49.
(34) Xu, J. J.; Zhao, H. K. An Eulerian formulation for solving partial differential equations along a moving interface. *J. Sci. Comput.* **2003**, *19*, 573−594.
(35) James, A. J.; Lowengrub, J. A surfactant conserving volume of fluid method for interfacial flows with insoluble surfactant. *J. Comput. Phys.* **2004**, *201*, 685−722.
(36) Hayashi, K.; Tomiyama, A. Effects of surfactant on terminal velocity of a Taylor bubble in a vertical pipe. *Int. J. Multiphase Flow* **2012**, *39*, 78−87.
(37) Liao, Y. C.; Franses, E. I.; Basaran, O. A. Deformation and breakup of a stretching liquid bridge covered with an insoluble surfactant monolayer. *Phys. Fluids* **2006**, *18*, 022101.
(38) Magnaudet, J.; Rivero, M.; Fabre, J. Accelerated flows past a rigid sphere or a spherical bubble. Part 1. Steady straining flow. *J. Fluid Mech.* **1995**, *284*, 97.
(39) Brackbill, J. U.; Kothe, D. B.; Zemach, C. A continuum method for modeling surface tension. *J. Comput. Phys.* **1992**, *100*, 335−354.
(40) Clift, R., Grace, J. R., Weber, M. E. *Bubbles, drops, and Particles*; Academic Press: New York, 1978.
(41) Mei, R.; Klausner, J. F.; Lawrence, C. J. A note on the history force on a spherical bubble at finite Reynolds number. *Phys. Fluids* **1994**, *6*, 418−420.
(42) Schiller, L.; Naumann, Z. A drag coefficient correlation. *Z. Ver. Deutsch. Ing.* **1935**, *77*, 318.
(43) Olbricht, W. L.; Kung, D. M. The deformation and breakup of liquid drops in low Reynolds number flow through a capillary. *Phys. Fluids A* **1992**, *4*, 1347−1354.
(44) Nath, B.; Biswas, G.; Dalal, A.; Sahu, K. C. Migration of a droplet in a cylindrical tube in the creeping flow regime. *Phys. Rev. E: Stat., Nonlinear, Soft Matter Phys.* **2017**, *95*, 033110.